

# Finite Element Method Based Design and Analysis of a Low Torque Ripple Double-Stator Switched Reluctance Motor

Tripurari Das Gupta<sup>1, 2</sup> and Kalpana Chaudhary<sup>1, \*</sup>

**Abstract**—Double-stator switched reluctance motors (DSSRMs) acquire attention because of their high torque/power generating capability compared to conventional and segmented rotor switched reluctance motors. One of the main limiting performance indices of such motors for industrial applications is its high torque ripple. This paper proposes a 12/10/12 pole DSSRM with an angular shift of half of the stroke angle between inner and outer stators. The respective phase windings of the inner and outer stators are parallelly excited with the same phase angle shift to reduce the torque ripple. Each rotor segment is constructed with a pair of half rotor segments that are isolated from each other through the insertion of a non-magnetic isolator between them. Firstly, the design hypothesis for a low torque ripple DSSRM has been presented; thereafter, some geometric modifications have been suggested and investigated to obtain a nearby response in the proposed DSSRM. The calculation of the width of the non-magnetic isolator, modification in the pole height of outer stator and modification in the arc angles of rotor segments/stator poles are discussed in detail. The effectiveness of the proposed motor is investigated through a 2D finite-element modelling and simulation in ANSYS/MAXWELL software. Simulation results show that the torque ripple is significantly reduced by 74.9% in the proposed DSSRM compared to the baseline DSSRM.

## 1. INTRODUCTION

Switched reluctance motors (SRMs) are known for their simple construction, absence of permanent magnet (PM), fault-tolerant capability, wide-speed operation, fewer devices, and low cost [1–4]. The property of the unipolar current excitation allows the designing of low-cost converters for SRMs with only one controlling switch per phase [5, 6]. SRMs have shown ability in electric vehicle applications [7], agricultural applications [8], aerospace applications [9], flywheel energy system [10], and household appliances [11, 12]. However, these machines still have issues of efficiency, lower torque/power density, high torque ripple, and high vibrations. Several researches have been reported in the literature to improve these parameters. The segmental rotor SRMs (SSRMs) having single-tooth windings attains improved flux linking per turn compared to full-pitch windings which subsequently improves its output torque [13]. The use of a high slot fill factor as well as high quality iron steel improves the efficiency of SRMs [14]. In the literature, mainly two types of torque ripple reduction techniques have been reported. Passive method refers to the structural design modification in the machine to reduce the torque ripple. In toothed SRMs (TSRMs), the structural modification in the leading edge of the rotor poles with fillet reduces the torque ripple [15]. The addition of a semi-oval auxiliary core on both sides of rotor tooth alleviates the torque ripple [16]. In active method, the shaping of phase currents through switching control is employed to reduce the torque ripple [17, 18]. The increase in phase number also lessens the torque ripple in SRMs. Deng et al. propose a torque control method with a novel 6-switch converter to

---

*Received 20 February 2021, Accepted 2 April 2021, Scheduled 7 April 2021*

\* Corresponding author: Kalpana Chaudhary (kchaudhary.eee@iitbhu.ac.in).

<sup>1</sup> Department of Electrical Engineering, Indian Institute of Technology (BHU), Varanasi 221005, India. <sup>2</sup> Department of Electrical and Electronics Engineering, Nalanda College of Engineering, Nalanda 803108, India.

further mitigate torque ripple in 6-phase SRMs [19]. In [20], a simplified control method for direct and simultaneous control of torque and force is reported for reducing the torque ripple/radial displacement in single-winding bearingless SRM.

DSSRMs having two stators and a segmented rotor further improve torque/power density. Bostanci et al. report that single-tooth winding DSSRM has comparable torque density to interior permanent magnet motor (IPM) [21]. However, it has lower efficiency and higher torque ripple. Most of the torque ripple reduction techniques used for conventional SRMs and SSRMs are also applicable to DSSRMs. A second-order sliding mode speed controller is presented to reduce the torque ripple of bearingless DSSRM in [22]. In [23], a static parametric analysis is investigated to optimise stator pole/rotor segment arc angles to achieve higher output torque and lower torque ripple in a 12/8/12 pole DSSRM. In this method, average torque is only calculated for  $15^\circ$  range from static torque profiles in place of  $22.5^\circ$ . This region includes the effective torque generation region, better considers excitation and demagnetisation process, and better differentiates the variation of arc angles. In [24] and [25], torque ripple reduction has been reported by displacing the adjacent rotor segments/poles in opposite directions in a dual-rotor single-stator axial flux SRM and in a double-sided axial flux SRM, respectively. A torque ripple reduction technique is reported with the angular shift of alternate rotor segments for single-tooth winding DSSRM in [26]. Asgar et al. propose a new design methodology for DSSRM by separating it into two SRMs, inner and outer rotor SRMs in [27].

This paper presents the design procedure of a 12/10/12 pole DSSRM with an angular shift of half of the stroke angle between inner and outer stators to mitigate the torque ripple. The respective phase windings of inner and outer stators are excited parallelly with the same phase shift. Each rotor segment consists of a pair of half rotor segments, which are isolated from each other with the insertion of a wider non-magnetic region between them. The width of this region is relatively wider than the usual width of the air-gap between stator and rotor surfaces. Due to the insertion of the non-magnetic region, the dimensions of the outer stator and half rotor segments alter considerably. Therefore, the modification in the pole height of outer stator and arc angles of rotor segments/stator poles are investigated and discussed in detail. A 2D finite-element model is established in ANSYS/MAXWELL software, and its simulated response is presented to investigate its effectiveness.

## 2. SINGLE-TOOTH WINDING DOUBLE-STATOR SRM

The constructional diagram of a 3-phase radial flux 12/10/12 pole single-tooth winding DSSRM is shown in Fig. 1. It consists of a segmental rotor situated between the inner and outer stators and helps to share their fluxes. Its 3D exploded view and 2D cross-sectional view, including winding polarities, are shown

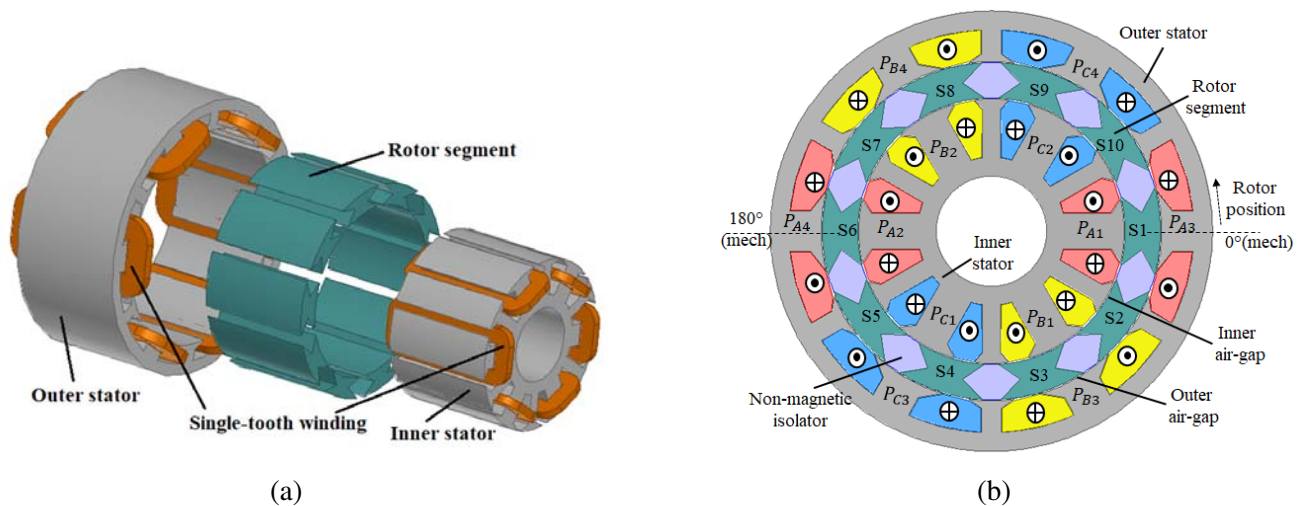


**Figure 1.** 12/10/12 pole single-tooth winding DSSRM. (a) 3D exploded view. (b) 2D cross-sectional view.

in Figs. 1(a) and 1(b), respectively. The rotor comprises 10 segments. These segments are isolated through a non-magnetic isolator between them. Each stator has alternatively wide and narrow poles of total 12 counts. Wide stator poles (viz.  $P_{A1}, P_{B1}, P_{C1}, \dots, P_{A4}, P_{B4}, P_{C4}$ ) are categorised as exciting poles, whereas narrow stator poles are categorised as auxiliary poles. Only exciting poles wound the phase windings. The auxiliary poles help for returning the fluxes of exciting poles via rotor segments. This winding topology is more fault-tolerant than the full-pitched winding case. The winding polarities shown in the figure avail the flux cancellation of inner and outer stator fluxes. It reduces the unaligned inductance and improves the energy conversion efficiency of motor [21]. Four different rotor segments try to magnetically align to a phase when it is excited (viz.  $S_1, S_2, S_6,$  and  $S_7$  for phase A). Therefore, the rotor starts rotating in the CCW direction if the phases are excited correctly in the sequence of A-B-C.

Figure 2 shows the pictorial representation of the flux distributions in DSSRM, at unaligned and aligned conditions, respectively. Unlike the full-pitched winding machines, the flux paths are shorter in this case, which increases the electrical utilisation of the motor. The figure also represents the phenomenon of the cancellation of inner and outer stator fluxes near the unaligned condition. Fig. 3 represents some of the design parameters of the DSSRM. In the figure,  $D_o, D_i,$  and  $D_r$  show the outer and inner diameters of the motor and average diameter of the rotor, respectively.  $\beta_r$  and  $\beta'_r$  are the arc angles of the inner and outer sides of the rotor segments, respectively.  $\beta_{exc}$  and  $\beta'_{exc}$  are the arc angles of inner and outer stator exciting poles, respectively.  $\beta_{aux}$  and  $\beta'_{aux}$  are the arc angles of inner and outer stator auxiliary poles, respectively.  $\beta_{ps}$  is the stator pitch angle. Inner and outer arc angles are considered the same in this case.

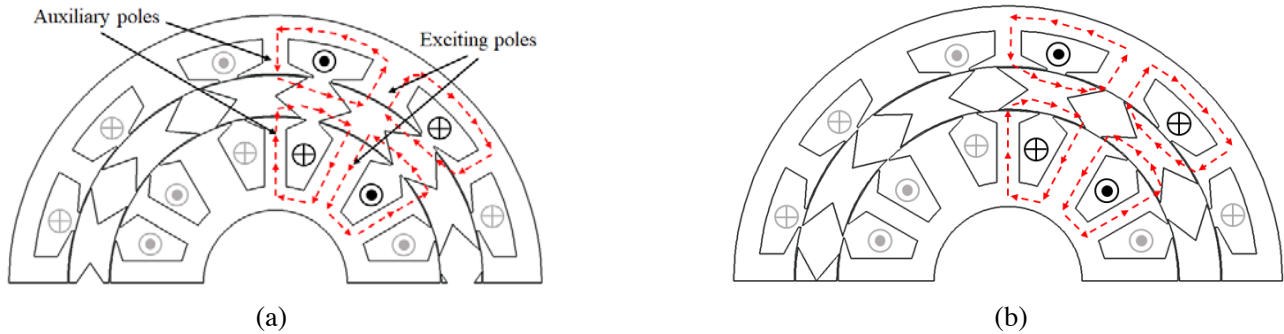


**Figure 2.** Flux distribution in DSSRM. (a) Unaligned condition. (b) Aligned condition.

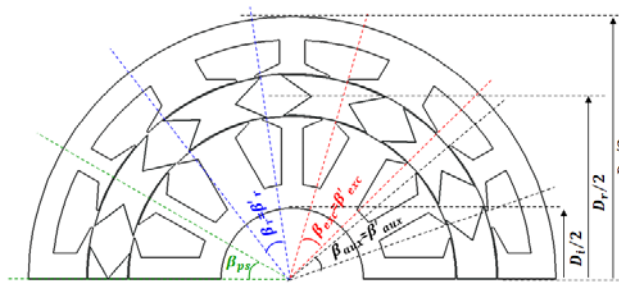


**Figure 3.** DSSRM design parameters.

One of the major limiting factors of the DSSRMs for their adaptation in industrial applications is their high torque pulsation. A 3-phase 12/10/12 pole single-tooth winding DSSRM has been taken as the baseline DSSRM in this paper to improve its torque pulsation behaviour. Table 1 enlists the design parameters of this baseline DSSRM. This baseline DSSRM is preserved as DSSRM1 in this paper. The dynamic response of the DSSRM1 has been simulated at the rated speed with the peak phase current of 30 A. The average torque ( $T_{avg}$ ), peak-to-peak ripple torque ( $T_{pk2pk}$ ), and % torque ripple ( $\% T_{ripple}$ )

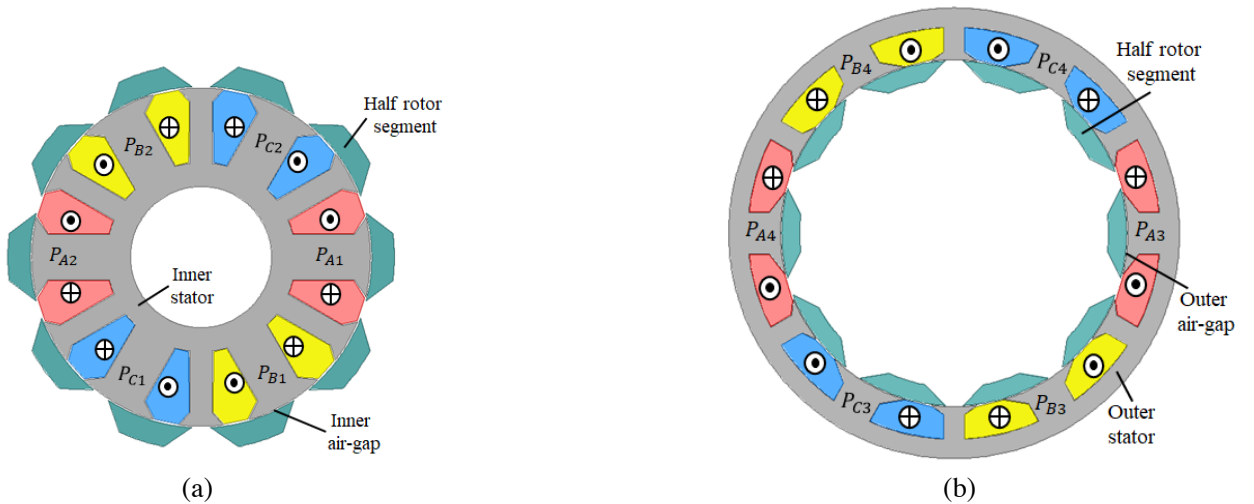
**Table 1.** Design specifications of the DSSRM1.

Number of inner stator poles/rotor segments/outer stator poles	12/10/12
Outer and inner diameter of outer stator	200 and 154 mm
Outer and inner diameter (shaft diameter) of inner stator	120 and 50 mm
Yoke height of inner and outer stator	8.5 mm
Axial length ( $l$ )	90 mm
Inner and outer arc angle of rotor segments ( $\beta_r$ and $\beta'_r$ )	$30^\circ$
Exciting and auxiliary pole arc angle ( $\beta_{exc}$ , $\beta_{aux}$ ) of inner stator	$27^\circ$ and $15^\circ$
Exciting and auxiliary pole arc angle ( $\beta'_{exc}$ , $\beta'_{aux}$ ) of outer stator	$27^\circ$ and $15^\circ$
Length of air-gaps( $l_g$ )	0.5 mm
Number of conductors/slot ( $N_{slot}$ )	54
Rated power	3.5 kW
Rated speed	1000 rpm
Peak phase current	30 A
Stroke angle and number of strokes per revolution	$12^\circ$ and 30

are 33.6 N-m, 41.6 N-m, and 123.8%, respectively. This investigation shows the presence of high torque ripples in this motor and divulges the need for further improvement in its torque pulsation behaviour.

### 3. DESIGN HYPOTHESIS FOR A LOW TORQUE RIPPLE DSSRM

A DSSRM can be considered a combination of two SRMs, inner SRM and outer SRM. Inner SRM consists of an inner stator, inner half part of the rotor, and inner stator coils. In the same way, outer SRM constitutes the outer stator, outer half part of the rotor, and outer stator coils. Fig. 4 shows these two SRMs, respectively. Fig. 5 shows the simulated dynamic response of these two SRMs at the rated speed with the peak phase current of 30 A. Figs. 5(a) and 5(b) show the phase currents and torque with rotor position for the inner and outer SRMs, respectively. It is seen that the angular separation between two adjacent torque peaks is  $12^\circ$ , whereas the separation between a torque peak and the adjacent torque dip is nearly  $6^\circ$  in both machines. These values are equal to the stroke angle and half of the stroke

**Figure 4.** Two separated parts of DSSRM1. (a) Inner SRM. (b) Outer SRM.

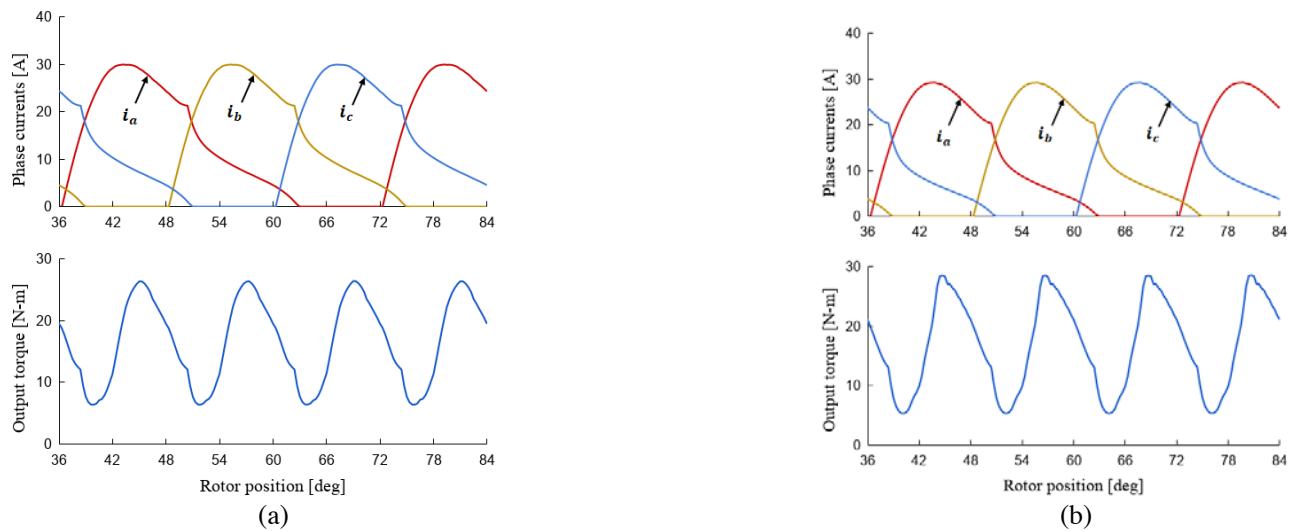


**Figure 5.** Dynamic response of two separated SRMs at rated speed. (a) Phase currents and torque of inner SRM. (b) Phase currents and torque of outer SRM.

angle, respectively. From this observation, it can be concluded that if both the SRMs are operated in a completely isolated condition with the phase shift  $6^\circ$ , the torque ripple can decrease inherently. The rising torque region of one SRM will overlap with the falling torque region of the other one, in this case, resulting in a comparatively lower torque ripple profile.

To validate the above theory, a hypothetical DSSRM of the same dimensions as DSSRM1 is modelled, and its performance is simulated through FEM analysis. Fig. 6 shows the constructional diagram of the hypothetical DSSRM. The outer stator of this machine has an angular shift of  $6^\circ$  in the direction of rotation with respect to the inner stator. Each rotor segment is divided into two halves, called half rotor segments. A hypothetical boundary is injected between them. The hypothetical boundary diminishes all the normal component of the flux falling on its surface and provides the complete magnetic isolation between the inner and outer magnetic circuits. The phase windings of the outer stator are excited parallelly with a delay of  $6^\circ$  (mech.) with respect to the phase windings of inner stator. This hypothetical machine is further renowned as DSSRM2 in this paper. The flux distribution in DSSRM2

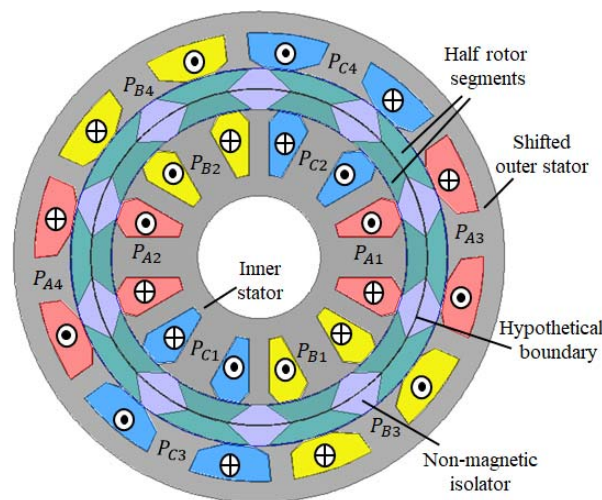


**Figure 6.** Structure of the hypothetical DSSRM2.

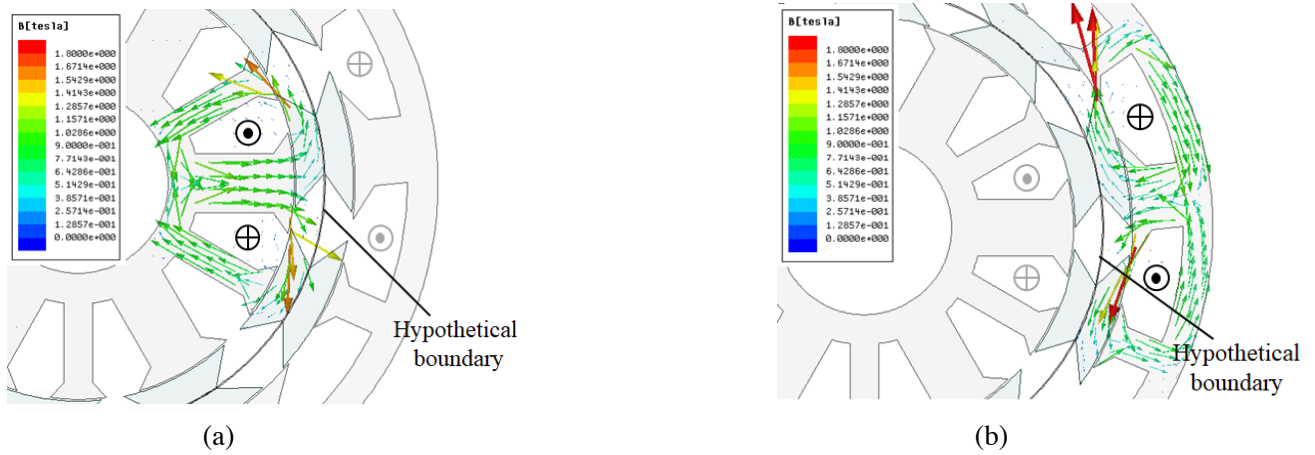


**Figure 7.** Flux distribution in DSSRM2. (a) Flux distribution with the excitation of inner stator winding at 90° (elec.) rotor position. (b) Flux distribution with the excitation of outer stator winding at 150° (elec.) rotor position.

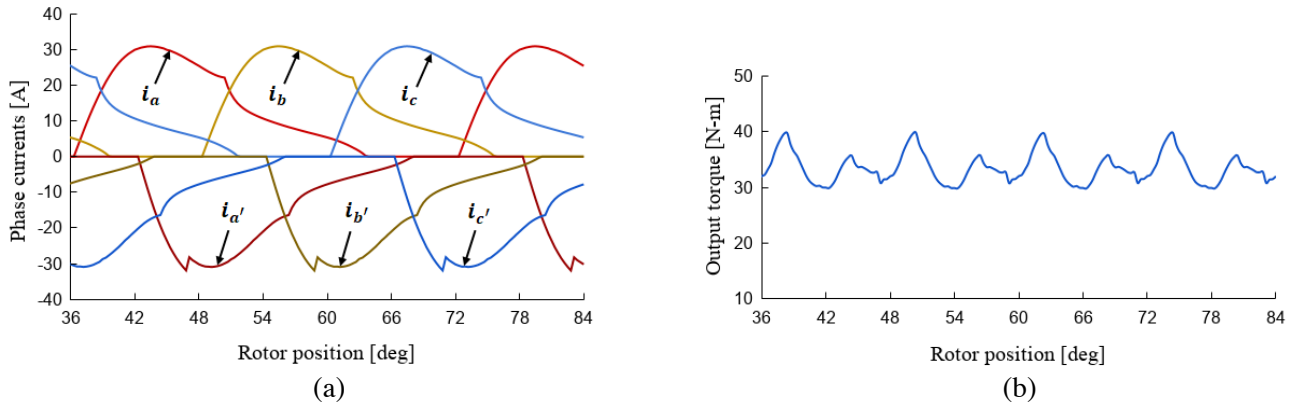


**Figure 8.** Response of DSSRM2 at rated speed. (a) Phase currents. (b) Dynamic torque.

is shown in Fig. 7 when the inner and outer stator phase windings are excited individually at 90° (elec.) and 150° (elec.) rotor positions, respectively. It is seen that because of the presence of the hypothetical boundary, the flux of the inner SRM does not link with the outer SRM and vice versa. In this way, the hypothetical boundary provides the complete magnetic isolation between the inner and outer magnetic circuits. Fig. 8 shows the simulated dynamic response of DSSRM2 at rated speed for the peak phase current of 30 A. In this figure,  $i_a$ ,  $i_b$ , and  $i_c$  are the phase currents of the inner stator windings whereas  $i_{a'}$ ,  $i_{b'}$ , and  $i_{c'}$  are the phase currents of outer stator windings. The values of  $T_{avg}$ ,  $T_{pk2pk}$ , and  $\% T_{ripple}$  are 33.5 N-m, 10.2 N-m, and 30.4%, respectively, in this case. This investigation shows that torque ripple in DSSRM2 is inherently low as compared to DSSRM1. However, this machine is practically not implementable because such a hypothetical boundary is not possible in reality. For implementing a nearby machine in the real platform, some geometric modifications and compromises are suggested and investigated in this paper. The design modifications for the proposed DSSRM containing the nearby response as in DSSRM2 are discussed in the next section.

#### 4. GEOMETRIC MODIFICATIONS IN THE PROPOSED DSSRM

As discussed in the previous section, the behaviour of the hypothetical boundary is to isolate the two magnetic circuits, i.e., inner and outer SRMs. However, during the implementation of the proposed

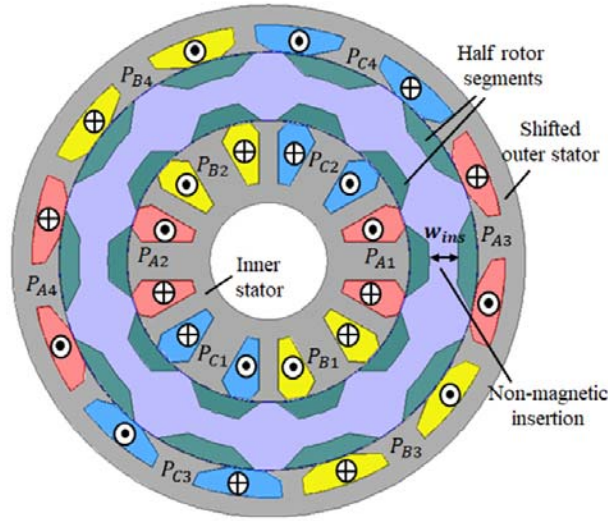


**Figure 9.** Initial structure of the proposed DSSRM.

DSSRM, considerable magnetic isolation can be provided between the two magnetic circuits by the insertion of a wider non-magnetic region between half rotor segments. Due to the insertion of this region, although the inner SRM remains same, the dimensions of the outer SRM alter considerably. This results in the alteration of its magnetic behaviour. Therefore, to meet the nearby response as in DSSRM2, some structural or geometric modifications are suggested and investigated in the proposed DSSRM. Fig. 9 shows the initial representation of the proposed DSSRM with the shifted outer stator and half rotor segments with a wider non-magnetic insertion of the width  $w_{ins}$  between them. The rotor segments can be assembled through a non-ferromagnetic cage, as suggested in [28]. This proposed machine will be further dealt with DSSRM3 in this paper. The process for the modifications in the DSSRM3 is discussed in further subsections.

#### 4.1. Modification in the Pole Height of Outer Stator

With the insertion of the non-magnetic isolator between the half rotor segments, the slot area of the outer stator increases for the same pole height. However, the slot area should be kept same before and after the insertion because it carries the same number of conductors of the same cross-sectional area. To achieve the same slot area pole height of the outer stator should be reduced in the latter case. Fig. 10 shows the inner radius ( $r$ ), pole height ( $h_{pso}$ ), and yoke height ( $h_{ys}$ ) of outer stator before the insertion of the isolator. These values change to  $(r + w_{ins})$ ,  $h'_{pso}$ , and  $h_{ys}$ , respectively, after the insertion of the isolator of the width  $w_{ins}$ . The condition for the same slot area in both cases is as follows:

$$\pi \left\{ (r + h_{pso})^2 - r^2 \right\} - A = \pi \left\{ (r + w_{ins} + h'_{pso})^2 - (r + w_{ins})^2 \right\} - A' \quad (1)$$

where  $A$  and  $A'$  are the cross-sectional areas covered by all the stator poles before and after the modification of the pole height of the outer stator. Fig. 10 clearly shows these areas with the shaded portion of the stator. Assuming that the same cross-sectional area is covered by the stator poles in both the cases (i.e.,  $A = A'$ ), the above condition is reduced to:

$$(r + h_{pso})^2 - r^2 = (r + w_{ins} + h'_{pso})^2 - (r + w_{ins})^2 \quad (2)$$

Eq. (2) can be used to calculate the approximate height of the outer stator poles  $h'_{pso}$  after the insertion of the non-magnetic isolator of the width  $w_{ins}$ . However, the exact height can be calculated through FEM analysis.

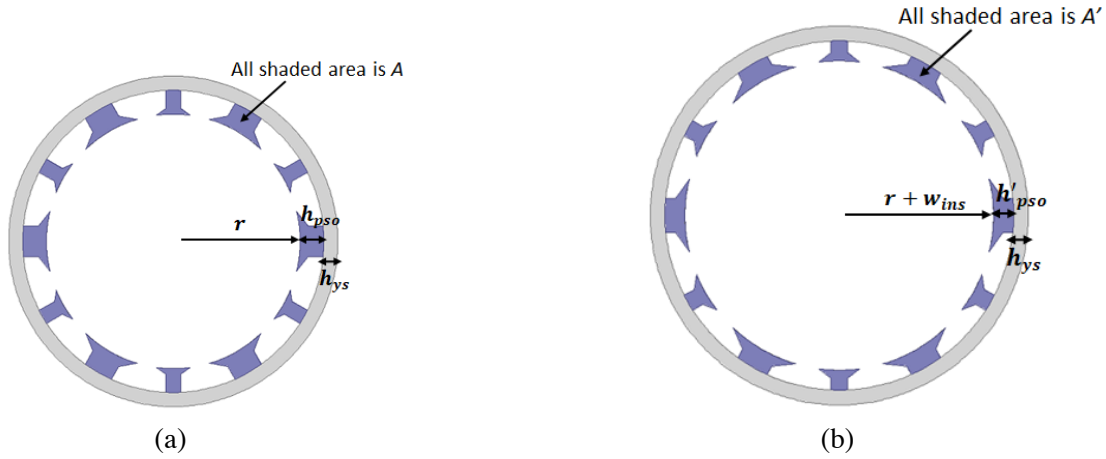


**Figure 10.** Modification in the pole height ( $h_{pso}$ ) of outer stator due to the insertion of the non-magnetic region. (a) Outer stator before insertion. (b) Outer stator after insertion ( $h'_{pso} < h_{pso}$ ).

#### 4.2. Calculation of the Width of the Non-Magnetic Region

The outer diameter of DSSRM3 increases with the insertion of the non-magnetic isolator between half rotor segments. There is a trade-off between the lower flux leakage between half rotor segments and smaller outer diameter of the motor. A larger value of  $w_{ins}$  results in a lower flux leakage, lower unaligned inductance, and further needs a lower DC link voltage for the rated operation. However, the outer diameter increases more in this case which will increase the size of the motor. Therefore, the value of  $w_{ins}$  should be selected with a better compromise between the flux leakage and outer diameter of the machine. Fig. 11(a) shows the flux density plot in DSSRM1 at unaligned rotor position for half of the peak phase current. A field calculator line is drawn passing through the middle of the rotor segments to calculate the leakage flux density on it. Fig. 11(b) shows the value of leakage flux density ( $B_{leak}$ ) calculated on this line between  $30^\circ$  and  $90^\circ$  mechanical positions of the motor. It is observed that the maximum value of  $B_{leak}$  is 66 mT. With the insertion of the non-magnetic isolator between the half rotor segments, it is considered that the maximum value of  $B_{leak}$  should not be much more than 70 mT. The value of  $B_{leak}$  in the middle of the half rotor segments at the unaligned position for the proposed DSSRM3 is given in Eq. (3)

$$B_{leak} = \frac{N_{slot} I_{ph} \mu_0}{2l_g + w_{ins}} \quad (3)$$

where  $I_{ph}$  is the phase current,  $N_{slot}$  the conductors/slot, and  $l_g$  the length of each air-gap. As per Eq. (3), the analytical value of  $w_{ins}$  for the considered leakage flux density of 70 mT is 13.5 mm.

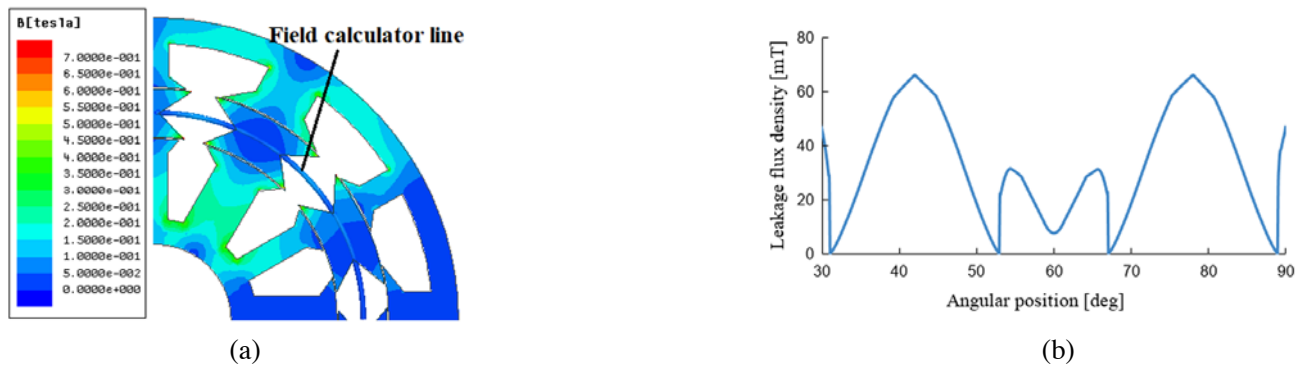


**Figure 11.** Calculation of leakage flux density in DSSRM1. (a) Flux density distribution at the unaligned position. (b) Leakage flux density calculated at the middle of the rotor segments.

**Table 2.** Comparative data for the variation of  $w_{ins}$ .

Width of the non-magnetic region ( $w_{ins}$ )	12 mm	13 mm	14 mm
Leakage flux density in mT	72.9	67.7	63.0
Outer diameter in mm	218	220	222
% Increase in outer diameter	9	10	11

However, the value of leakage flux density, the outer diameter of the motor, and the % increase in outer diameter are calculated through FEM analysis for the variation of  $w_{ins}$  with a parametric step of 1 mm. Table 2 gives the results of this analysis. It is seen that the leakage flux density decreases with an increase in  $w_{ins}$ ; however, the outer diameter of the motor also increases. The value of  $w_{ins}$  for the considered leakage flux density of 70 mT will lie between 12 and 13 mm. Therefore, the calculation is further extended for the value of  $w_{ins}$  of 12.5 mm. The values of leakage flux density and outer diameter are 70.1 mT and 219 mm, respectively, which are adaptable. This value of  $w_{ins}$  is further considered in this study.

### 4.3. Modification in the Arc Angle of Outer Rotor Segments/Stator Poles

With the insertion of the non-magnetic region between half rotor segments, the arc lengths of the outer half rotor segments and stator poles increase for the same arc angle before the insertion, which increases the flux linkage and inductance value of outer stator winding at all angular positions. The change in the inductance profile will lead to the difference between desired and actual responses. Therefore, the modifications in the arc angle of outer half rotor segments ( $\beta'_r$ ) and stator poles ( $\beta'_{exc}$ ,  $\beta'_{aux}$ ) are investigated to achieve the desired response.

In the presented analysis, the design of a hypothetical DSSRM, as shown in Fig. 6, is presented which has a reduced torque ripple. Now the objective of this paper is to optimize the dimensions  $\beta'_r$ ,  $\beta'_{exc}$ , and  $\beta'_{aux}$  (as shown in Fig. 3) of the proposed DSSRM in such a way as to achieve the torque characteristics which nearly match that of the hypothetical machine. In order to achieve this, the inductance profile of the proposed machine must match that of the hypothetical machine, i.e., the absolute error between their phase inductance profiles should be minimum. Thus, the cost function for the given optimization problem can be obtained as

$$C = \min \left( \int |L_{DSSRM2} - L_{DSSRM3}| \right) \quad (4)$$

The cost value is calculated in rotor position range between  $13^\circ$  and  $22^\circ$ . This range is considered because it is the effective torque generating region, better considers the excitation and demagnetization process, and better differentiates the variation of pole arc angles. The various design variables used for optimization are shown in Fig. 3, and their ranges of variation are given in Table 3.

**Table 3.** List of variables defined for optimization.

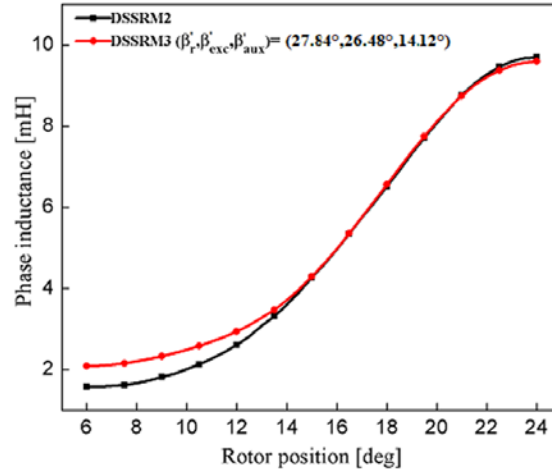
Variable	Range
$\beta'_r$	$30^\circ - 26^\circ$
$\beta'_{exc}$	$28^\circ - 24^\circ$
$\beta'_{aux}$	$16^\circ - 12^\circ$

The discussed optimization problem can be easily solved on ANSYS Electromagnetics platform using optimetrics analysis. A 2-D model of the machine is prepared on the software, and the optimization setup is formulated in which the cost function given in Eq. (4) is defined using the setup calculation. The optimization condition is set to minimize. To perform this optimization analysis, Genetic Algorithm method is used. The optimized values of the various parameters obtained are given in Table 4.

**Table 4.** Optimized values of the parameters.

Variable	Optimized Value
$\beta'_r$	27.84°
$\beta'_{exc}$	26.48°
$\beta'_{aux}$	14.12°

The optimized dimensions are used in the proposed machine model for verification of the inductance profile. The FEM analysis of the Machine model with optimized dimensions is performed, and the analysis results of the inductance profile are found to match that of the hypothetical machine between 13° and 22° rotor positions as shown in Fig. 12. Therefore, these optimized values are considered to further analyze the dynamic response of the proposed machine.

**Figure 12.** Matching of inductance profile of DSSRM2 and DSSRM3 between 13° to 22° rotor position.

## 5. FINITE-ELEMENT MODELLING AND SIMULATION RESULTS

Table 1 deals with the design parameters of the DSSRM1. The modifications in the parameters for the proposed DSSRM3 are discussed in Section 4. The 2D finite-element modelling is carried out, owing to its high accuracy. The electromagnetic responses are achieved using ANSYS/MAXWELL software. This software tool is very effective to analyse the flux path, field lines, flux density, and vector potential for electromagnetic analysis [29]. The steps involved in the FEM study are modelling, material assignment, boundary assignment, meshing and excitation. ‘steel-1008’ available in the software library is used for the stator and rotor cores with 0.4 mm lamination width. An odd symmetry boundary is used for the creation of hypothetical boundary in DSSRM2. The driving circuits used to simulate the dynamic response of the DSSRM1 and DSSRM3 are asymmetric half-bridge converters which utilise two power switches per phase winding and provide maximum control flexibility. However, as per specific application by compromising with control flexibility, other known converters can also be utilised, which require less than two switches per phase winding [30]. Hysteresis control with the bandwidth of  $\pm 0.5$  A is considered to limit the phase current. The turn-on and turn-off angles for the phases are 0° and 14.3° (mech.), respectively. Eq. (5) and Eq. (6) give the details to measure the torque ripple and efficiency ( $\eta$ ).

$$T_{\text{ripple}} = T_{\text{pk2pk}}/T_{\text{avg}} \quad (5)$$

$$\eta = P/(P + P_L) \quad (6)$$

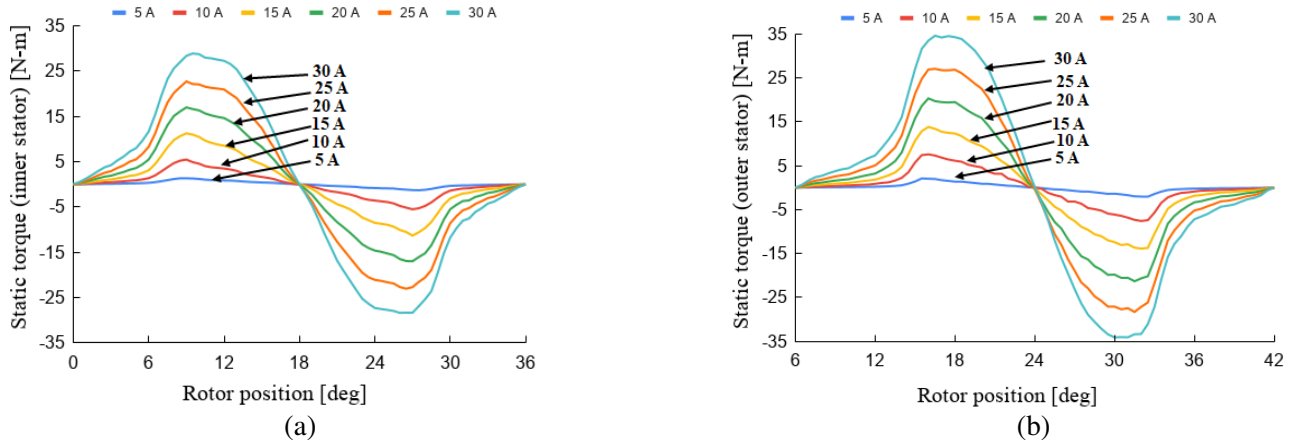


**Figure 13.** Static torque profiles for inner and outer stator. (a) Static torque for inner stator. (b) Static torque for outer stator.

**Table 5.** Comparative data for DSSRM1 and DSSRM3 at rated speed.

	DSSRM1	DSSRM3
RPM	1000	1000
Phase turn-on angle in degree (mech.)	0	0
Phase turn-off angle in degree (mech.)	14.3	14.3
$T_{avg}$ in N-m	33.6	33.7
$T_{pk2pk}$ in N-m	41.6	10.5
$T_{ripple}$ in %	123.8	31.1
Core loss in W	93	109
Copper loss in W	385	370
Rated efficiency in %	88.0	88.0

where  $P$  is output power excluding the mechanical losses, and  $P_L$  includes losses through core and copper loss.

Figures 13(a) and 13(b) show the static torque profiles for the inner and outer stators, respectively. It is shown that the outer stator’s torque is peakier than the inner stator for the same value of phase current. This will add some peaky response in the resultant output torque. Fig. 14 represents the flux density distribution in the proposed model at the rated operating condition and at  $90^\circ$  (elec.) and  $150^\circ$  (elec.) rotor positions, respectively. Fig. 15 shows the simulated dynamic responses of DSSRM1 and DSSRM3 at rated speed. For high output torque and low torque ripple, the phase current overlapping technique is used in both cases [31]. Fig. 15(a) shows the variation of phase currents, i.e.,  $i_a$ ,  $i_b$ , and  $i_c$ , and the output torque of the DSSRM1. The value of  $T_{avg}$ ,  $T_{pk2pk}$ , and %  $T_{ripple}$  are 33.6 N-m, 41.6 N-m, and 123.8%, respectively, in this case. It reveals the presence of a high torque ripple in this motor. Fig. 15(b) shows the dynamic response of the optimized DSSRM3 for the rated operating condition.  $i_a$ ,  $i_b$ , and  $i_c$  are the phase currents of the inner stator windings whereas  $i_{a'}$ ,  $i_{b'}$ , and  $i_{c'}$  are the phase currents of the outer stator windings. The values of  $T_{avg}$ ,  $T_{pk2pk}$ , and %  $T_{ripple}$  are 33.7 N-m, 10.5 N-m, and 31.1%, respectively, in this case. It discloses that the torque ripple is significantly reduced in this case. Table 5 deals with the comparative data of DSSRM1 and DSSRM3 for rated speed. The total loss through copper and core loss are 478 W and 479 W in the baseline and proposed DSSRM, respectively. The copper loss is lower in the proposed DSSRM than the baseline DSSRM because of the slight decrease in required per phase average and rms currents. However, the core loss is higher than that of the baseline DSSRM because of the increase in leakage flux. The efficiencies are comparable in

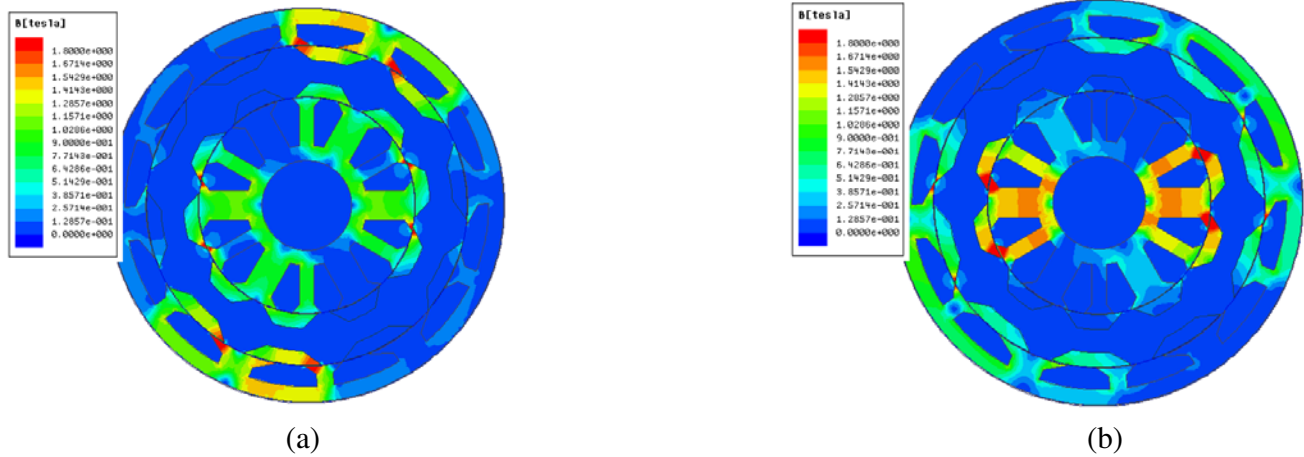


**Figure 14.** Flux density distribution in the proposed model at  $90^\circ$  (elec.) and  $150^\circ$  (elec.) rotor position with respect to phase A and rated operating condition. (a)  $90^\circ$  (elec.) rotor position. (b)  $150^\circ$  (elec.) rotor position.

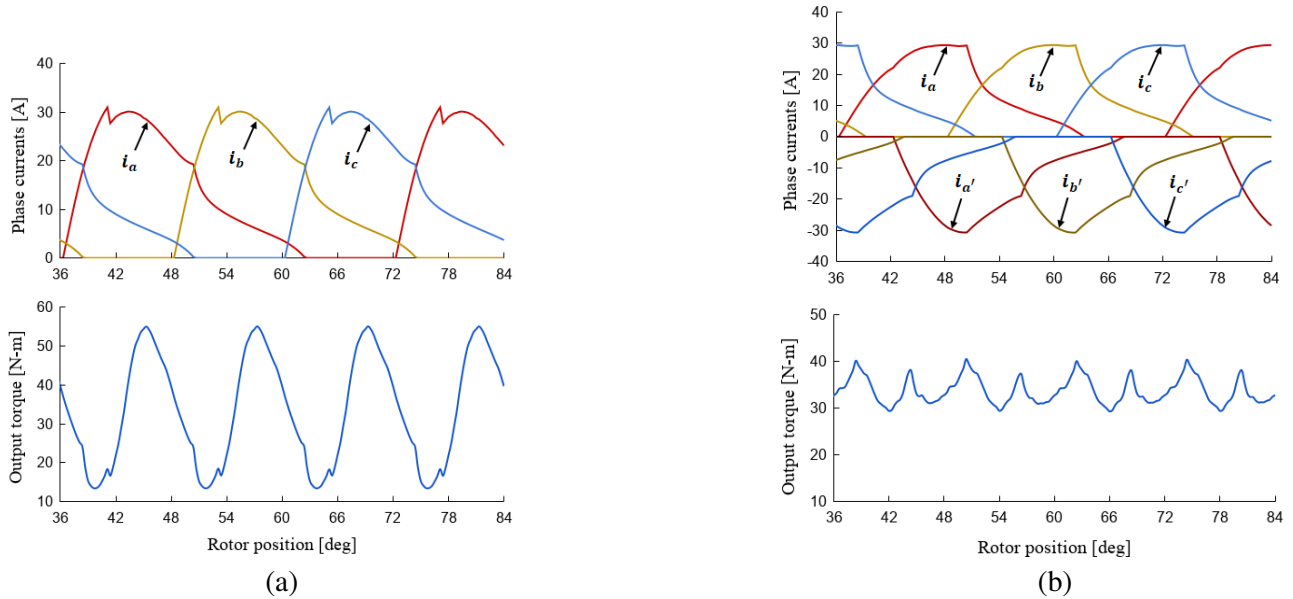


**Figure 15.** Response of the DSSRM1 and DSSRM3 at rated speed. (a) Phase currents and torque waveforms of DSSRM1. (b) Phase currents and torque waveforms of DSSRM3.

the two cases.

Figure 16 compares the dynamic torques and torque ripple frequencies for both the motors at rated speed. Fig. 16(a) shows that the peak-to-peak torque ripple is relatively low in the case of the proposed DSSRM; subsequently, torque ripple is reduced by 74.9% compared to DSSRM1. There are some peaky responses in the output torque of the proposed motor near  $39^\circ$ ,  $51^\circ$ ,  $63^\circ$ , and  $75^\circ$  rotor positions. This is because of the peaky static torque profiles of the outer stator as seen in Fig. 13. Fig. 16(b) shows the harmonics analysis of torque ripple frequencies for both the motors. The DC or average values of the torques are 33.6 N-m and 33.7 N-m for the baseline and proposed DSSRM, respectively. The fundamental and most dominant harmonics is 500 Hz. The magnitudes of these harmonics are 59.0% and 6.0% of DC value for baseline and proposed DSSRM, respectively. Therefore, this harmonic is reduced by 53.0% in the proposed motor. It prevails that low-frequency torque ripples are reduced in the case of the proposed motor. Fig. 17 shows the resultant force working on the whole motor body of

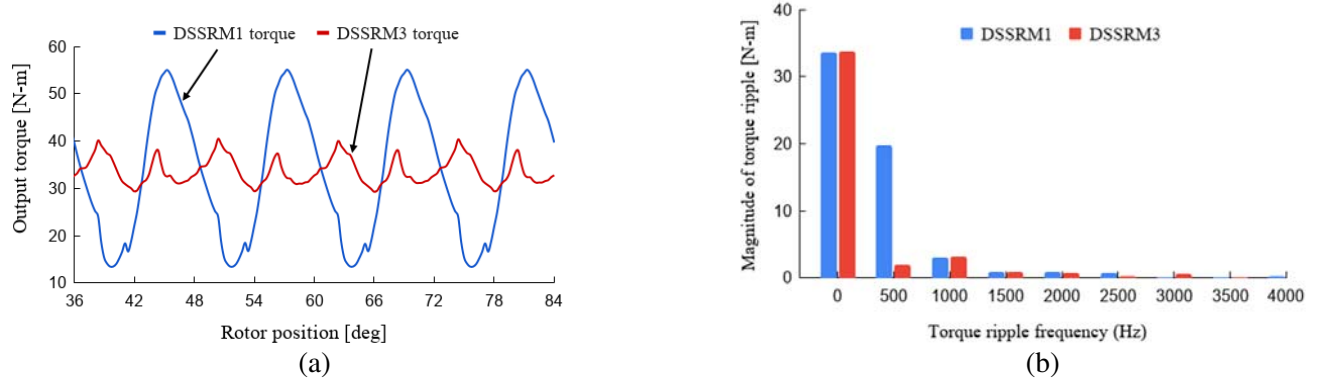


**Figure 16.** Comparison of the torques of DSSRM1 and DSSRM3 at rated speed. (a) Dynamic torques. (b) Magnitudes of torque ripple harmonics.

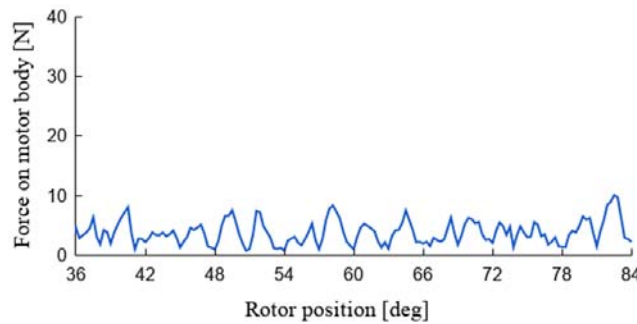


**Figure 17.** Resultant force working on the whole motor body of DSSRM3.

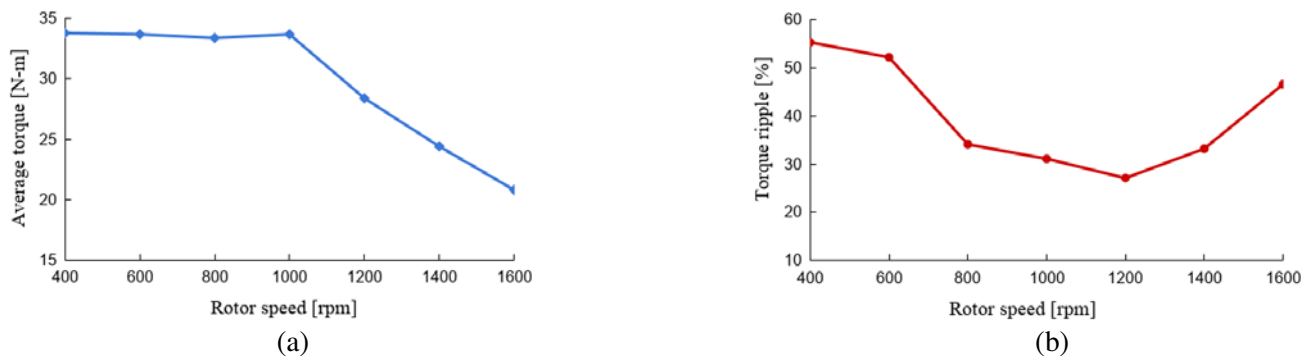


**Figure 18.** Output torque and torque ripple of proposed DSSRM with rotor speed. (a) Output torque. (b) Torque ripple.

the proposed DSSRM at rated condition. The average value of this force is 3.6 N which is ignorable. In the case of the baseline DSSRM, this value is 2.0 N.

Figure 18(a) represents the output torque of the proposed motor with the variation of rotor speed. Below the base speed, the output torque is maintained constant by maintaining the average value of the phase current nearly constant through the hysteresis current control technique. In SRMs, output power decreases above the base speed. This is because, with the increase in rotor speed, the back EMF increases, and the time provided to increase the phase current also decreases. This reduces the phase current and subsequently reduces the output power above the base speed. Phase current advancing technique is employed to maintain the output power above the base speed [32]. In this technique,

phases are energised before the actual turn-on position. It increases the phase current and maintains the constant output power above the base speed. Fig. 18(b) shows the torque ripples with the variation of rotor speed. It shows that comparatively lower torque ripples occur near rated speed between 800 and 1400 rpm. This is because, in this speed range, the falling torque region and rising torque region of one stator are better compensated by the other one. The minimum value of torque ripple is 27.1% which occurs at 1200 rpm rotor speed. The above observations envisage that such motor can be employed in the applications where a lower torque ripple is required at a higher speed region.

## 6. CONCLUSION

This paper presents the finite-element modelling and analysis of a low torque ripple 12/10/12 pole DSSRM. In the proposed DSSRM, the outer stator is angularly shifted with half of the stroke angle, i.e.,  $6^\circ$  in the direction of rotation. The respective phase windings of the outer stator are excited parallelly with a delay of  $6^\circ$  compared to the inner ones. Each rotor segment is composed of two half rotor segments. A wider non-magnetic isolator is inserted between the half rotor segments to sufficiently isolate them. The torque ripple in the proposed DSSRM is compared with that of baseline DSSRM. It is observed that the proposed DSSRM has a significant reduction in torque ripple. During the design procedure of the proposed motor, firstly, a hypothetical DSSRM is discussed with a significantly lower value of torque ripple. Thereafter, geometric modifications are investigated to meet the nearby response in the proposed DSSRM as in the hypothetical machine. The modifications carried out in the proposed DSSRM are the insertion of the non-magnetic isolator between half rotor segments, change in the pole height of outer stator, and change in arc angle of outer half rotor segments and stator poles. The procedures for these design modifications are discussed in detail. A 2D FEM model of the proposed motor with optimized dimensions is established in ANSYS/MAXWELL software, and its response is simulated. The torque ripples in the baseline and proposed DSSRM are 123.8% and 31.1%, respectively. Therefore, the torque ripple is reduced by 74.9% in the proposed DSSRM for the rated operating condition. The efficiencies are comparable in the two cases. The proposed motor can be employed for low torque ripple applications.

## REFERENCES

1. Chiba, A., K. Kiyota, N. Hoshi, M. Takemoto, and S. Ogasawara, "Development of a rare-earth-free SR motor with high torque density for hybrid vehicles," *IEEE Transactions on Energy Conversion*, Vol. 30, No. 1, 175–182, March 2015.
2. Gerada, D., A. Mebarki, N. L. Brown, C. Gerada, A. Cavagnino, and A. Boglietti, "High-speed electrical machines: Technologies, trends, and developments," *IEEE Transactions on Industrial Electronics*, Vol. 61, No. 6, 2946–2959, June 2014.
3. Ling, X., B. Li, L. Gong, Y. Huang, and C. Liu, "Simulation of switched reluctance motor drive system based on multi-physics modeling method," *IEEE Access*, Vol. 5, 26184–26189, 2017.
4. Han, G., H. Chen, and G. Guan, "Low-cost SRM drive system with reduced current sensors and position sensors," *IET Electric Power Applications*, Vol. 13, No. 7, 853–862, July 2019.
5. Sun, Q., J. Wu, C. Gan, Y. Hu, N. Jin, and J. Guo, "A new phase current reconstruction scheme for four-phase SRM drives using improved converter topology without voltage penalty," *IEEE Transactions on Industrial Electronics*, Vol. 65, No. 1, 133–144, January 2018.
6. Krishnan, R., S.-Y. Park, and K. Ha, "Theory and operation of a four-quadrant switched reluctance motor drive with a single controllable switch—the lowest cost four-quadrant brushless motor drive," *IEEE Transactions on Industry Applications*, Vol. 41, No. 4, 1047–1055, July–August 2005.
7. Gan, C., J. Wu, Q. Sun, W. Kong, H. Li, and Y. Hu, "A review on machine topologies and control techniques for low-noise switched reluctance motors in electric vehicle applications," *IEEE Access*, Vol. 6, 31430–31443, 2018.
8. Mishra, A. K. and B. Singh, "Self-governing single-stage photovoltaic water pumping system with voltage balancing control for a four-phase SRM drive," *IET Electric Power Applications*, Vol. 14, No. 1, 119–130, January 2020.

9. Borg Bartolo, J., M. Degano, J. Espina, and C. Gerada, "Design and initial testing of a high-speed 45-kW switched reluctance drive for aerospace application," *IEEE Transactions on Industrial Electronics*, Vol. 64, No. 2, 988–997, February 2017.
10. Ho, C., J. Wang, K. Hu, and C. Liaw, "Development and operation control of a switched-reluctance motor driven flywheel," *IEEE Transactions on Power Electronics*, Vol. 34, No. 1, 526–537, January 2019.
11. Liang, J., L. Jian, G. Xu, and Z. Shao, "Analysis of electromagnetic behavior in switched reluctance motor for the application of integrated air conditioner on-board charger system," *Progress In Electromagnetics Research*, Vol. 124, 347–364, 2012.
12. Isobe, K., K. Nakamura, and O. Ichinokura, "A consideration of high speed SR motor for electric power tools," *Journal of the Magnetics Society of Japan*, Vol. 38, No. 5, 194–198, 2014.
13. Mecrow, B. C., E. A. El-Kharashi, J. W. Finch, and A. G. Jack, "Segmental rotor switched reluctance motors with single-tooth windings," *IEE Pro. — Electric Power Applications*, Vol. 150, No. 5, 591–599, September 9, 2003.
14. Hayashi, H., K. Nakamura, A. Chiba, T. Fukao, K. Tungpimolrut, and D. Dorrell, "Efficiency improvements of switched reluctance motors with high-quality iron steel and enhanced conductor slot fill," *IEEE Transactions on Energy Conversion*, Vol. 24, No. 4, 819–825, December 2009.
15. Li, Y., S. Ravi, and D. C. Aliprantis, "Tooth shape optimization of switched reluctance motors for improved torque profiles," *Power & Energy Society General Meeting*, 1–7, July 26–30, 2015.
16. Jing, L. and J. Cheng, "Research on torque ripple optimization of switched reluctance motor based on finite element method," *Progress In Electromagnetics Research M*, Vol. 74, 115–123, 2018.
17. Li, Q., A. Xu, L. Zhou, and C. Shang, "A deadbeat current control method for switched reluctance motor," *Progress In Electromagnetics Research Letters*, Vol. 91, 123–128, 2020.
18. Wang, S., Z. Hu, and X. Cui, "Research on novel direct instantaneous torque control strategy for switched reluctance motor," *IEEE Access*, Vol. 8, 66910–66916, 2020.
19. Deng, X., B. Mecrow, H. Wu, and R. Martin, "Design and development of low torque ripple variable-speed drive system with six-phase switched reluctance motors," *IEEE Transactions on Energy Conversion*, Vol. 33, No. 1, 420–429, March 2018.
20. Cao, X., J. Zhou, C. Liu, and Z. Deng, "Advanced control method for a single-winding bearingless switched reluctance motor to reduce torque ripple and radial displacement," *IEEE Transactions on Energy Conversion*, Vol. 32, No. 4, 1533–1543, December 2017.
21. Bostanci, E., M. Moallem, A. Parsapour, and B. Fahimi, "Opportunities and challenges of switched reluctance motor drives for electric propulsion: A comparative study," *IEEE Trans. Transport. Electric.*, Vol. 3, No. 1, 58–75, March 2017.
22. Chen, C., H. Guo, and G. Zhang, "SOSM direct torque and direct suspension force control for double stator bearingless switched reluctance motor," *Progress In Electromagnetics Research C*, Vol. 96, 179–192, 2019.
23. Sun, Q., J. Wu, C. Gan, C. Shi, and J. Guo, "DSSRM design with multiple pole arcs optimization for high torque and low torque ripple applications," *IEEE Access*, Vol. 6, 27166–27175, 2018.
24. Madhavan, R. and B. G. Fernandes, "Performance improvement in the axial flux-segmented rotor-switched reluctance motor," *IEEE Transactions on Energy Conversion*, Vol. 29, No. 3, 641–651, September 2014.
25. Kermanipour, M. J. and B. Ganji, "Modification in geometric structure of double-sided axial flux switched reluctance motor for mitigating torque ripple," *Canadian Journal of Electrical and Computer Engineering*, Vol. 38, No. 4, 318–322, 2015.
26. Gupta, T. D., K. Chaudhary, R. M. Elavarasan, R. K. Saket, I. Khan, and E. Hossain, "Design modification in single-tooth winding double-stator switched reluctance motor for torque ripple mitigation," *IEEE Access*, Vol. 9, 19078–19096, 2021.
27. Asgar, M., E. Afjei, and H. Torkaman, "A new strategy for design and analysis of a double-stator switched reluctance motor: Electromagnetics, FEM, and experiment," *IEEE Trans. Magn.*, Vol. 51, No. 12, 1–8, December 2015.

28. Asgar, M. and E. Afjei, "Radial force reduction in a new flat-type double-stator switched reluctance motor," *IEEE Transactions on Energy Conversion*, Vol. 31, No. 1, 141–149, March 2016.
29. Gecer, B. and N. F. O. Serteller, "Understanding switched reluctance motor analysis using ANSYS/Maxwell," *2020 IEEE 29th International Symposium on Industrial Electronics (ISIE)*, 446–449, Delft, Netherlands, 2020.
30. Miller, T. J. E., *Switched Reluctance Motors and Their Control*, CRC Press, London, U.K., 1993.
31. Mademlis, C. and I. Kioskeridis, "Performance optimisation in switched reluctance motor drives with online commutation angle control," *IEEE Transactions on Energy Conversion*, Vol. 18, No. 3, 448–457, September 2003.
32. Rekik, M., M. Besbes, C. Marchand, B. Multon, S. Loudot, and D. Lhotellier, "Improvement in the field-weakening performance of switched reluctance machine with continuous mode," *IET Electric Power Applications*, Vol. 1, No. 5, 785–792, September 2007.